Downshift of the Ni d band center over Ni nanoparticles *in situ* confined within an amorphous silicon nitride matrix

Norifumi Asakuma[a], Shotaro Tada[a,b], Tomoyuki Tamura[c], Erika Kawaguchi[a], Sawao Honda[a], Toru Asaka[a], Assil Bouzid[d], Samuel Bernard[d], Yuji Iwamoto[a]

[a]; Department of Life Science and Applied Chemistry, Graduate School of Engineering, Nagoya Institute of Technology, Nagoya, Japan

[b]; Department of Metallurgical and Materials Engineering, Indian Institute of Technology Madras, Chennai, India

[c]; Department of Applied Physics, Graduate School of Engineering, Nagoya Institute of Technology, Nagoya, Japan

[d]; IRCER, CNRS, Univ. Limoges, Limoges, France

Experimental section

Chemicals

Commercially available poly(vinylmethyl-*co*-methyl)silazane (Durazane®1800, Sanwa Kagaku, Corp., Shizuoka, Japan), nickel chloride ($NiCl_2$, 98 % purity, Sigma-Aldrich Japan, Tokyo, Japan), and super-anhydrous toluene (99.5 % purity, Wako Pure Chemical Industries, Ltd., Osaka, Japan) were used without further purification.

Synthesis of Ni-modified single source precursor

Prior to the synthesis for the single source precursor, $NiCl_2$ was exposed to a flow of NH_3 (300 $mLmin^{-1}$) at 120 °C for 2 h to afford $Ni(NH_3)_6Cl_2$ as a monomeric Ni precursor. The XRD pattern of the synthesized Ni complex (purple powder) was identical to that of $Ni(NH_3)_6Cl_2$ (JCPDS No. 04-010-8016, Figure S1).

All the reactions and handling of the chemicals for single source precursor synthesis were carried out under an inert atmosphere of pure argon (Ar) using standard Schlenk-line and grove box techniques. The synthesis of the Ni-modified single source precursor (**NiPSZ**) for the Ni nanoparticles-dispersed amorphous silicon carbonitride composite was performed at the atomic ratio of Ni in $Ni(NH_3)_6Cl_2$ to Si in polysilazane (Ni/Si) = 0.05. In a typical experiment, a two-neck round-bottom flask equipped with a magnetic stirrer was charged with polysilazane (4.025 g, 65 mmol) and $Ni(NH_3)_6Cl_2$ (0.705 g, 3.04 mmol, Ni/Si =0.05). Then, anhydrous toluene (36 mL) was added to the mixture at room temperature. The resulting purple-colored mixture was refluxed at 115 °C for 15 h under flowing Ar with stirring. During refluxing, the color of the mixture changed from purple to black, indicating the occurrence of chemical reactions between polysilazane and Ni precursors. After the mixture was cooled down to room temperature, the toluene was removed under vacuum at 50 °C to

afford the **NiPSZ**. As a reference sample, single source precursor derived from Ni-free polysilazane, which is labeled as **PSZ**, was synthesized the same way as the synthesis of **NiPSZ**.

Conversion to polymer-derived Ni/a-SiCN, Ni/a-Si₃N₄ and Ni/a-SiO₂ nanocomposites

The synthesized **NiPSZ** was firstly converted to Ni nanoparticles-dispersed amorphous silicon carbonitride (**Ni/a-SiCN**) composite by heat treatment under N_2 flowing (200 mL min^{-1}) at 400 °C for 4 h with the ramping rate of 5 °C min^{-1} and subsequent heat treatment at 500 °C for 2 h with the ramping rate of 5 °C min^{-1}. Then, the **Ni/a-SiCN** was converted to the following two different composite systems, Ni nanoparticles-dispersed amorphous silicon nitride (**Ni/a-Si₃N₄**) and amorphous silicon dioxide (**Ni/a-SiO₂**) systems by differing the appropriate anneal treatment atmosphere, respectively. For the **Ni/a-Si₃N₄** system, the **Ni/a-SiCN** system was annealed under NH_3 flowing (200 mL min^{-1}) at 600 °C for 3 h with the ramping rate of 10 °C min^{-1}. After the holding time, the flowing gas was switched from NH_3 to N_2, and the furnace was cooled to room temperature. On the other hand, for the **Ni/a-SiO₂** synthesis, the **Ni/a-SiCN** was once converted to nickel oxide nanoparticle-dispersed amorphous silica (labeled as **NiO/a-SiO₂**) by annealing under an ambient atmosphere at 550 °C for 1.5h with a ramping rate of 10 °C min^{-1}. Subsequently, the NiO in the **NiO/a-SiO₂** composite was reduced to afford the **Ni/a-SiO₂** by heat treatment under 10 % H_2-Ar flowing (200 mL min^{-1}) at 400 °C for 2 h with a ramping rate of 10 °C min^{-1}. As a comparison, the samples without Ni loading were synthesized in the same way, and hereafter these samples were labeled as **a-Si₃N₄** and **a-SiO₂**, respectively.

Characterization

The synthesized single source precursors were characterized by an attenuated total reflection flourier transform infrared (ATR-FTIR) spectroscopy using FTIR spectrometer (FT/IR-4200IF, JASCO Corporation, Tokyo, Japan) with a diamond prism under an incidence angle of 45° loaded in an ATR attachment (ATR PRO 550S-S/570S-H, JASCO Corporation, Tokyo, Japan). The ATR-FTIR spectra were collected at a resolution of 4 cm^{-1} with a cumulative number of 128 and the spectra were normalized by δSi-CH₃ peak at 1254 cm^{-1}.

To investigate the chemical bonding states of the single source precursors, Raman spectra were recorded (Model inVia, Renishaw, UK) using a single mode solid laser with a wavelength of 633 nm and a power of 25 mW for Raman excitation. The Raman spectra were normalized to the strongest peak in each spectrum by the strongest peak.

The pyrolysis behavior of synthesized single source precursors was studied by simultaneous thermogravimetric (TG) and mass spectroscopic (MS) analyses (Model STA7200, Hitachi High Technologies Ltd., Tokyo, Japan) coupled with a quadrupole mass-spectrometry (Model JMS-Q1050GC, JEOL Ltd., Tokyo, Japan). The measurements were performed under flowing He (100 mL min^{-1}) with a heating rate of 10 °C min^{-1}.

The chemical composition of the pyrolyzed samples was calculated according to following

equation:

$$wt\%(Si+Ni+Cl)=100\% - wt\%(C) - wt\%(N) - wt\%(O) \quad (1)$$

where the carbon (C) content was measured using a carbon analyzer (non-dispersive infrared method, Model CS844, LECO Corporation, Michigan, USA), and the oxygen (O) and nitrogen (N) contents were measured using an oxygen-nitrogen hydrogen analyzer (inert-gas fusion method, Model EMGA-930, HORIBA, Ltd., Kyoto, Japan), while the Si, Ni, Cl contents were analyzed by the energy dispersive X-ray spectroscopy (EDS) mounted on a scanning electron microscope (SEM, Model JSM-6010LA, JEOL Ltd., Tokyo, Japan).

The textural properties of the pyrolyzed samples were evaluated by measuring N_2 adsorption and desorption isotherms at -196 °C under relative pressures ranging from 0 to 0.99 (Model Belsorp Max, BEL Japan Inc., Osaka, Japan).

The powder X-ray diffraction (XRD) pattern analysis of the pyrolyzed samples was performed on a flat sample stage using Ni-filtered CuKα radiation (Model X'pert, Philips, Amsterdam, The Netherlamds). XRD patterns were collected with a scan rate of 4.7 ° min^{-1} in the regions of 10 to 90°. The average crystallite size (L) of metal nickel formed *in situ*, was obtained from the Scherrer equation as follows:

$$L=K\lambda/\beta\cos\theta \quad (2)$$

where λ is the X-ray wavelength in nanometer, K is a constant related to crystallite shape, generally applied as 0.9, and β is the peak width of the diffraction peak at half maximum height in radian. The β in this study was collected from the diffraction peak at 44.4°.

To investigate the surface electronic nature of **Ni/a-SiO$_2$ and Ni/a-Si$_3$N$_4$** samples, X-ray photoelectron spectroscopic (XPS) measurements were performed using an X-ray Photoelectron Spectrometer (PHI Quantes, ULVAC-PHI, Inc., Japan) with an Al Kα X-ray source and 100 μm for X-ray beam diameter. The C1s peak of adventitious carbon (284.8 eV) was used as a reference for estimating the binding energy. Deconvolution of each spectrum was performed using the Igor pro 7 fitting engine. A program package of X-ray Photoelectron Spectroscopy Tools (XPST) was used in this study. Non-linear curve fitting was performed using the Pseudo-Voigt function with a fixed Gauss(G) Lorentz(L) ratio of G: L=7:3.

Transmission electron microscope (TEM) observations were performed on the pyrolyzed samples in a JEOL JEM-ARM200F operated at an accelerating voltage of 200 kV. The Ni average size and size distribution histogram were obtained from 50 particles using Image J program (NIH free software ver.1.52a).

Hydrogen adsorption and desorption properties of Ni/a-SiO$_2$ and Ni/a-Si$_3$N$_4$

Temperature-programmed-desorption of hydrogen (H$_2$-TPD) of **Ni/a-SiO$_2$** and **Ni/a-Si$_3$N$_4$** samples was performed to investigate the catalytic support effect on the interaction strength between nickel and adsorbed hydrogen using a catalyst analyzer equipped with TCD (Model BELCAT-A,

MicrotracBEL Corp., Osaka, Japan). The setup of the career and feed gases flow was fixed to 50 cm^3 min^{-1}. A channel-shaped quartz tube with an inner diameter of 8 mm was used, and before each sample (0.1 g) loading, the glass wool was packed at a neck of the reactor for a sample to be vertically contacted with flowing gases. Temperature-programmed heating was always managed with a thermocouple that was touched on the sample. Before collecting the H$_2$-TPD profile, the sample was activated at 415 °C under flowing pure H$_2$ for 1h, then switched to Ar flowing for 1h, followed by cooling to 50 °C under flowing Ar. Subsequently, the sample was exposed to pure H$_2$ at 50 °C for 1h, then switched to Ar flowing, and maintained at 50 °C for 1h to remove the physisorbed H$_2$ species. Finally, the H$_2$-TPD profile was recorded under flowing Ar with various ramping rates.

Computational calculation

For all spin-polarized density functional theory calculations, the Quantum ESPRESSO package [1,2] was used. Electron-core interactions were described using the projector augmented wave (PAW) pseudopotentials [3] with 2s2p of N and O, 3s3p of Si, and 3d4s4p of Ni treated as valence electrons. Electronic exchange-correlation interactions were evaluated by the generalized gradient approximation (GGA) formulated by Perdew, Burke, and Ernzerhof (PBE) [4]. In all calculations, kinetic energy cutoffs used to represent the electron wave function and charge density are 544 eV (40 Ry) and 6802 eV (500 Ry), respectively. The Fermi surface was broadened using a gaussian smearing parameter of 0.204 eV. The Brillouin zone was sampled by the Monkhorst-Pack k-point grid [5], with the reciprocal lattice spacing ≈ 0.2 Å^{-1} for structural relaxation. For the structural relaxation, all the atoms were allowed to relax with a minimum error threshold of 1.36×10^{-5} eV for self-consistency until the total energy change and the force on atoms were below the thresholds of 1.36×10^{-3} eV and 0.026 eV Å^{-1}. For optimized structures, we analyzed the projected density of states (pDOS) by non-self-consistent field calculations with the reciprocal lattice spacing ≈ 0.1 Å^{-1}.

The lattice constant for the optimized fcc Ni was 3.515 with the magnetic moment of 0.61 μ_B per atom. The lattice constants for the optimized hexagonal β-Si$_3$N$_4$ and trigonal α-SiO$_2$ (α-quartz) are a = b = 7.652, c = 2.922 Å and a = b = 4.931, c = 5.432 Å, respectively. These values are in good agreement with other theoretical and experimental ones [6-8].

For the investigation of interfacial phenomena, the supercells for Ni/ β-Si$_3$N$_4$ and Ni/ α-SiO$_2$ were constructed using the Ni (111) slab model since this plane is the most stable one in fcc Ni [9]. For the Ni (111)/ β-Si$_3$N$_4$ interface model, the Ni (111) slab model with 7 layers was laid on the β-Si$_3$N$_4$ (001) slab model with 9 layers. Similarly, for the Ni (111)/ α-SiO$_2$ interface model, the Ni (111) slab model with 7 layers was laid on the O-terminated α-SiO$_2$ (001) slab model with a thickness of 4 units. It is well known that the strain effect affects the electronic properties of transition metals, especially for the d band center [10]. To investigate and discuss the effect of interfacial Ni-N and Ni-O interactions on the electronic nature of Ni, the lateral side of supercells was fixed at the lattice constant of the Ni (111) slab model. The mismatch of lattice parameters was estimated by the following

equation,

$$\text{mismatch} = \frac{b_{Ni} - b_\alpha}{b_{Ni}} \quad (3)$$

where b is the lateral size of the slab, and subscript α denotes the β-Si$_3$N$_4$ or α-SiO$_2$. The mismatches for Ni (111)/ β-Si$_3$N$_4$ and Ni (111)/ α-SiO$_2$ interface models are -2.6 and $+0.8$ %, respectively. As a reference, Ni (111) slab model was modeled by 7 layers with the 3×3 lateral units. The vacuum region with a 10 Å thickness was set to prevent the interaction between slabs as shown in Figure S8.

The d band center (ε_d) is evaluated by the following formula,

$$\varepsilon_d\sigma = \frac{\int_{-\infty}^{E_F} E D_d^\sigma(E) dE}{\int_{-\infty}^{E_F} D_d^\sigma(E) dE} \quad (4)$$

where D_d^σ is PDOS on the d-states on the Ni, σ is the majority spin ($\uparrow$) or minority spin ($\downarrow$), E is the energy, and E_F is the Fermi energy of the system [11,12]

The projected crystal orbital Hamilton populations (pCOHP) were calculated by using the Local-Orbital Basis Suite Toward Electronic-Structure Reconstruction package (LOBSTER) [13,14]. The average pCOHP of interfacial Ni-N and Ni-O bonds with a bond length within 2.0 Å was shown in each supercell.
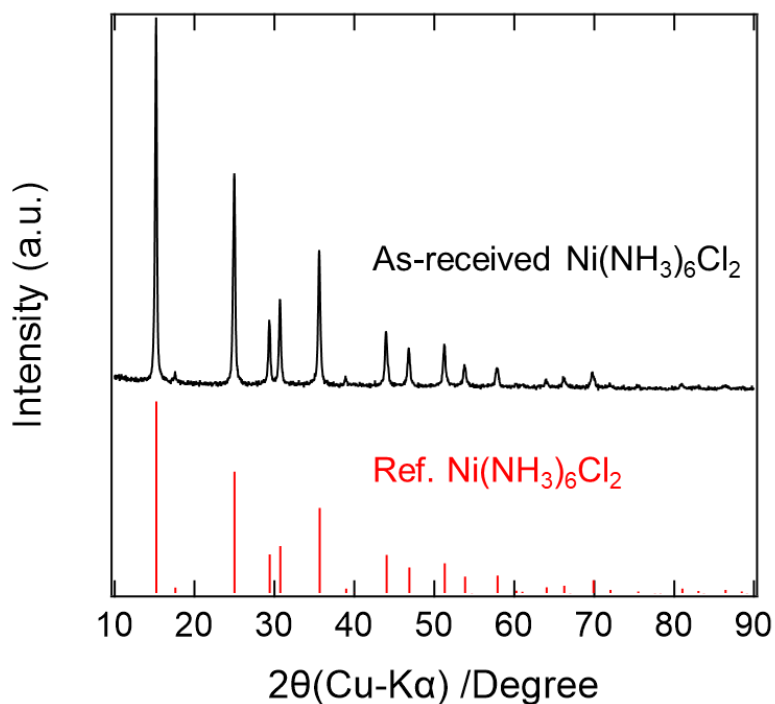
Figure S1. Powder X-ray diffraction patterns of as-received $Ni(NH_3)_6Cl_2$ (black line). The verticle red lines represent the reference of $Ni(NH_3)_6Cl_2$ (JCPDS No. 04-010-8016).

Table S1. The intensity ratio of typical absorption bands for as-received **PSZ** and **NiPSZ** samples.

| Sample	νN-H/δSi-CH$_3$	νSi-H/δSi-CH$_3$
NiPSZ	0.15	0.52
PSZ	0.36	0.88
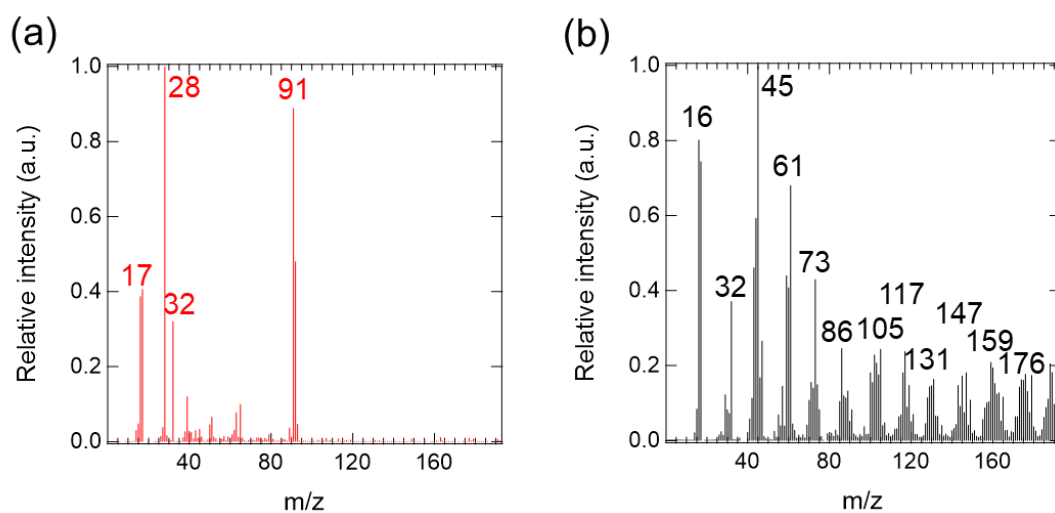
Figure S2. Monitoring of evolved gaseous species at 100−500 °C for **NiPSZ** (red lines) and **PSZ** (black lines) samples by the simultaneous MS analysis.
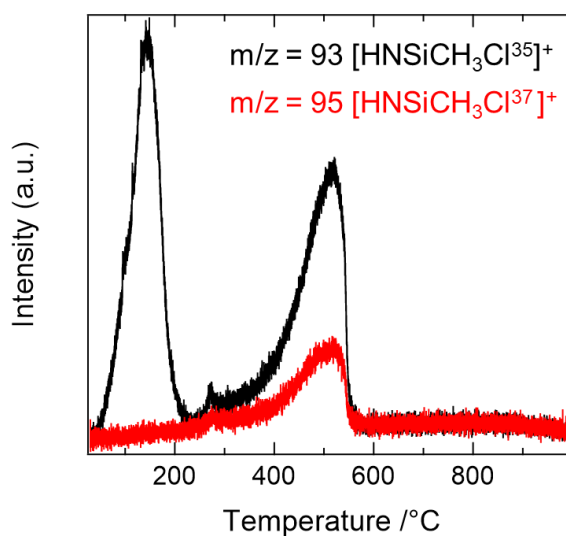
Figure S3. Selected mass fragments of **NiPSZ** monitored continuously during the measurements. At about 400−550 °C, the intensity ratio of fragments with m/z for 93 and 95 corresponds to about 3 in accordance with the Cl isotopic ratio ($^{35}Cl/^{37}Cl = 3.14$ [15]). Therefore, the gaseous products are identified as the monochlorosilane species.
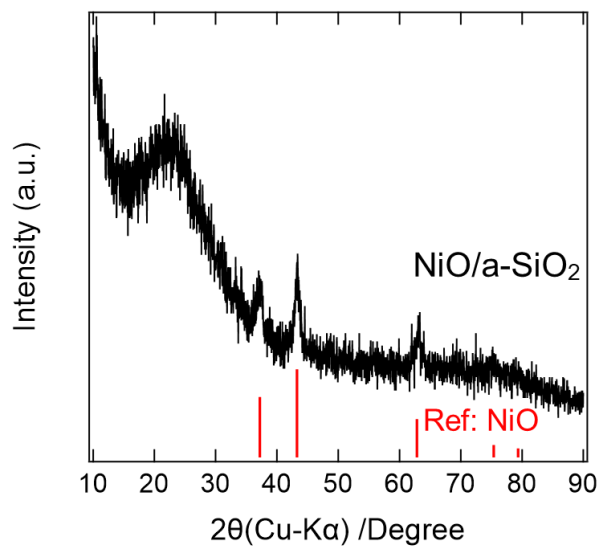
Figure S4. Powder X-ray diffraction patterns of as-received **NiO/SiO** (black line). The verticle red lines represent the reference of NiO (JCPDS No. 01-078-0423).
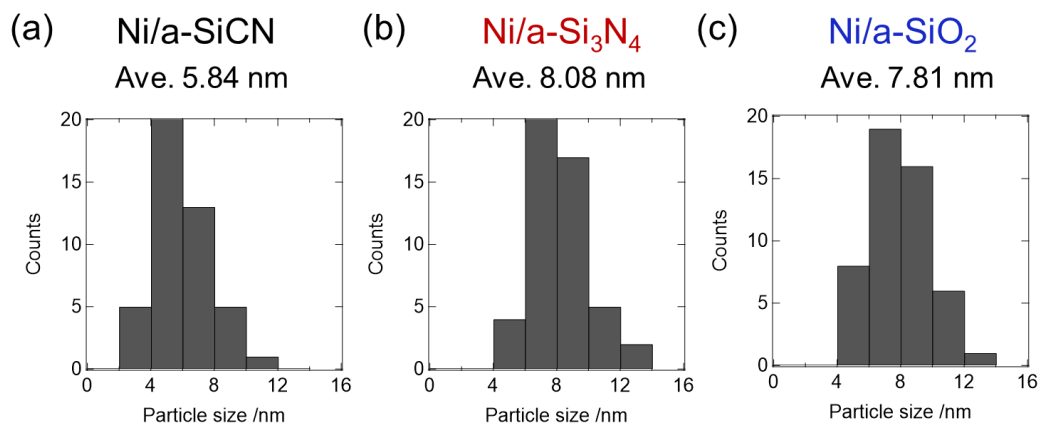

Figure S5. Ni size distribution histogram (statistics on 50 Ni nanoparticles) of **Ni/a-SiCN**, .**Ni/a-Si₃N₄,** and **Ni/a-SiO₂,**
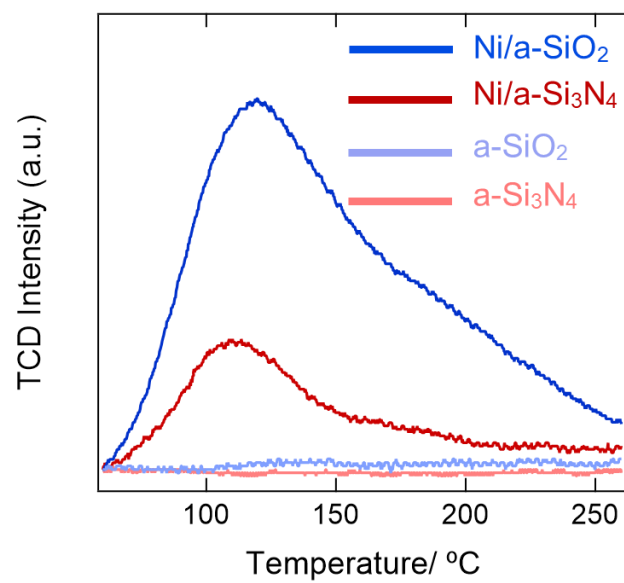
Figure S6. Comparison of H_2-TPD profiles for the **Ni/a-Si$_3$N$_4$** (dark-red line), **Ni/a-SiO$_2$** (dark-blue line), **a-Si$_3$N$_4$** (light-red line), and **a-SiO$_2$** (light-blue line) samples after H_2 exposure at 50 °C by the temperature ramping rate: 13 °C min^{-1}. These profiles are normalized by the sample weight.
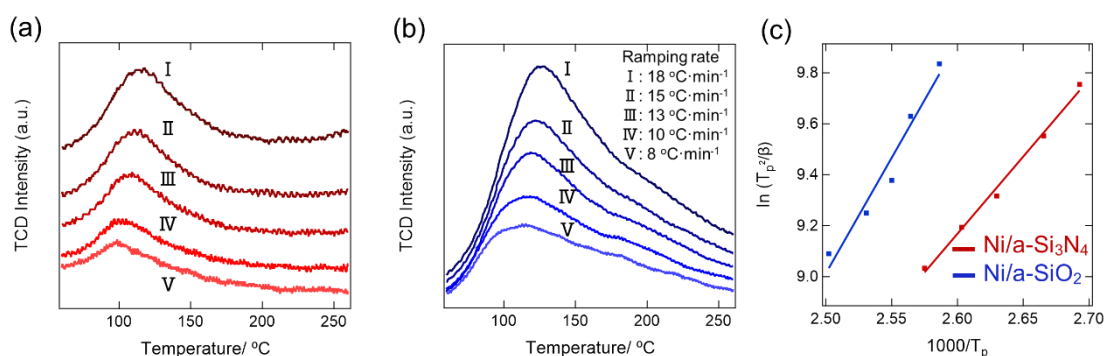
Figure S7. Reproduction test of the **Ni/a-Si₃N₄** and **Ni/a-SiO₂** synthesized in the same manner for calculating the activation energy for H_2 desorption. H_2-TPD profiles for the **Ni/a-Si₃N₄** (a), and **Ni/a-SiO₂** (b) samples after H_2 exposure at 50 °C by varying the temperature ramping rate: 18, 15, 13, 10, and 8 °C min^{-1}, respectively. (c) Plot of $\ln((T_p)^2/\beta)$ against $1/T_p$ for **Ni/a-Si₃N₄** (dark-red line) and **Ni/a-SiO₂** (dark-blue line) samples. The activation energy for H_2-desorption of **Ni/a-Si₃N₄** and **Ni/a-SiO₂** samples were estimated from the slope of the straight line (50.3 and 75.3 kJ mol^{-1}, respectively).
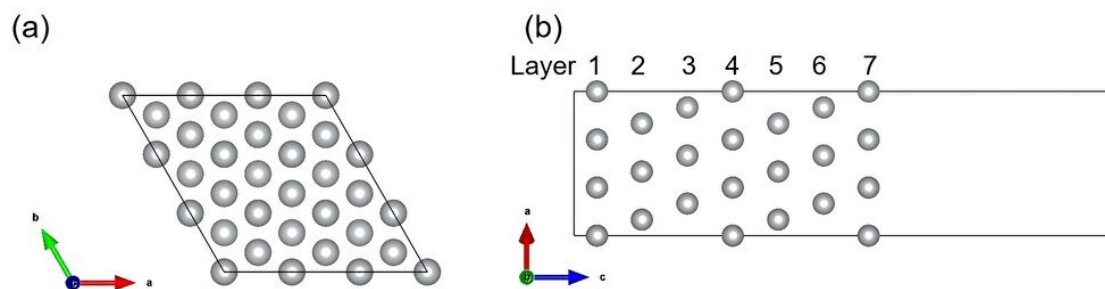
Figure S8. (a) Top view and (b) lateral side of the Ni (111) slab model. Layer 1 and 7 of Ni correspond to the surface region, while Layer 4 corresponds to the bulk region.
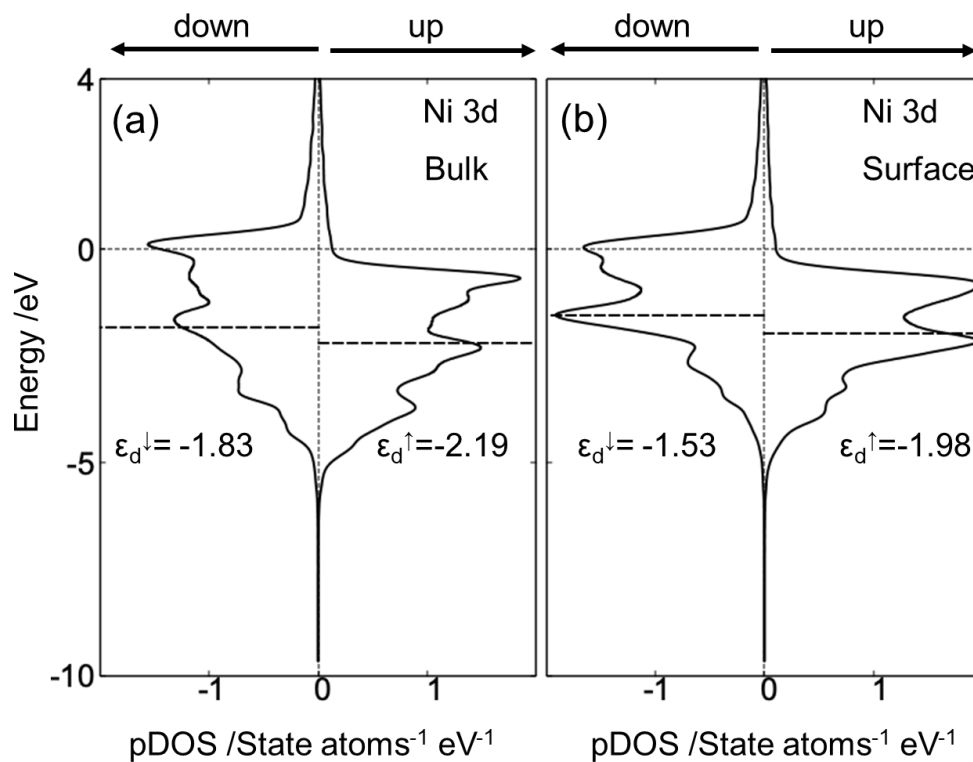

Figure S9. pDOS of Ni 3d orbitals of the bulk (a) and surface (b) region for the Ni (111) slab model. Fermi level is set to the energy of 0 eV. The d band center ε_d for spin-up (↑) and that for spin-down (↓) of Ni are depicted by a dashed line in pDOS.

Reference

1. P. Giannozzi, S. Baroni, N. Bonini, M. Calandra, R. Car, C. Cavazzoni, D. Ceresoli, G. L. Chiarotti, M. Cococcioni, I. Dabo, A. Dal Corso, S. de Gironcoli, S. Fabris, G. Fratesi, R. Gebauer, U. Gerstmann, C. Gougoussis, A. Kokalj, M. Lazzeri, L. Martin-Samos, N. Marzari, F. Mauri, R. Mazzarello, S. Paolini, A. Pasquarello, L. Paulatto, C. Sbraccia, S. Scandolo, G. Sclauzero, A. P. Seitsonen, A. Smogunov, P. Umari and R. M. Wentzcovitch, *J. Phys. Condens. Matter*, 2009, **21**, 395502.

2. P. Giannozzi, O. Andreussi, T. Brumme, O. Bunau, M. B. Nardelli, M. Calandra, R. Car, C. Cavazzoni, D. Ceresoli, M. Cococcioni and others, *J. Phys. Condens. Matter*, 2017, **29**, 465901.

3. P. E. Blöchl, *Phys. Rev. B*, 1994, **50**, 17953–17979.

4. P. Perdew, K. Burke and M. Ernzerhof, *Phys. Rev. Lett.*, 1996, **77**, 3865–3868.

5. H. J. Monkhorst and J. D. Pack, *Phys. Rev. B*, 1976, **13**, 5188–5192.

6. G. Kresse and J. Hafner, *Surf. Sci.*, 2000, **459**, 287–302.

7. V. M. Bermudez, *Surf. Sci.*, 2020, **691**, 121511.

8. K. Mizokami, A. Togo and I. Tanaka, *Phys. Rev. B*, 2018, **97**, 1–10.

9. Y. N. Wen and J. M. Zhang, *Solid State Commun.*, 2007, **144**, 163–167.

10. Xia, Z.; Guo, S. Strain Engineering of Metal-Based Nanomaterials for Energy Electrocatalysis. *Chem. Soc. Rev.* **2019**, *48*, 3265–3278, doi:10.1039/c8cs00846a.

11. M. Paßens, V. Caciuc, N. Atodiresei, M. Moors, S. Blügel, R. Waser and S. Karthäuser, *Nanoscale*, 2016, **8**, 13924–13933.

12. I. Del Rosal, M. Mercy, I. C. Gerber and R. Poteau, *ACS Nano*, 2013, **7**, 9823–9835.

13. R. Nelson, C. Ertural, J. George, V. L. Deringer, G. Hautier and R. Dronskowski, *J. Comput. Chem.*, 2020, **41**, 1931–1940.

14. S. Maintz, V. L. Deringer, A. L. Tchougréeff and R. Dronskowski, *J. Comput. Chem.*, 2016, **37**, 1030–1035.

15. M. Berglund and M. E. Wieser, *Pure Appl. Chem.*, 2011, **83**, 397–410.